Journal of Solid State Chemistry **165,** 25–34 (2002)
doi:10.1006/jssc.2001.9485, available online at http://www/idealibrary.com on IDEAL®

# Preparation and Characterization of *N*-4-Nitrophenyl-L-prolinol Nanocrystals in Sol–Gel Matrices

N. Sanz,* J. Zaccaro,* L. Delmotte,† C. Le Luyer,‡ and A. Ibanez*,[1]

*Laboratoire de Cristallographie, CNRS, UPR 5031 associée à l'Université J. Fourier et à l'INPG, BP 166, 38042 Grenoble Cedex 09, France; †Laboratoire des Matériaux, Minéraux ENSCMu, 3 rue Alfred Werner, 68093 Mulhouse Cedex, France; and ‡Laboratoire de Physico-Chimie des Matériaux Luminescents, CNRS UMR 5620, Université Claude Bernard Lyon I, 43 bd du 11 Novembre 1918, 69622 Villeurbanne Cedex, France
E-mail: ibanez@polycnrs-gre.fr

Received June 5, 2001; in revised form November 22, 2001; accepted December 21, 2001

**Organic nanocrystals of *N*-4-nitrophenyl-L-prolinol (NPP) have been grown in sol–gel matrices prepared from silicon alkoxide precursors. Our process is based on the control of the nucleation and growth kinetics of the dye in the pores of dense gels. Nanocomposites gel–glasses are obtained with a high optical quality due to the small size of the nanocrystals (10–20 nm). Differential scanning calorimetry experiments evidenced clearly the melting point of NPP nanocrystals, which is registered 51°C above that of NPP powder. Micro-Raman and solid state NMR spectroscopies allowed us to demonstrate that our nanocrystallization process does not chemically modify NPP molecules. We specified also the nature of interactions existing between the NPP nanocrystals and the xerogels. These strong interactions, which explain the important increase of the melting point of the nanocrystals in comparison to the NPP powder, are hydrogen bonds between nitro groups of NPP and uncondensed silanol functions of the silicate network.** © 2002 Elsevier Science (USA)

*Key Words:* **nanocrystals; hybrid organic–inorganic materials; sol–gel; nanocomposite; confined nucleation; *N*-4-nitrophenyl-L-prolinol; quadratic nonlinear optical materials; aggregation; differential scanning calorimetry; Raman spectroscopy; NMR spectroscopy.**

## 1. INTRODUCTION

In the past two decades, there has been great interest in the enhancement of optical nonlinearity of metallic (Au, Ag, Fe, etc.) and semiconductor (I–VII, II–V, and III–V) nanoparticles (1). This interest is motivated by strong confinement effects on electron–hole excitations, i.e., Wannier excitons. Such effects are not expected in organic crystals where Frenkel excitons are mainly localized on one molecule. This could explain why the preparation and study of organic aggregates was practically unexplored (2, 3). In addition, despite the very wide range of optical properties of organic nanocrystals, they have attracted little attention because of the difficulties associated with their structural characterization.

Indeed, organic phases exhibit unique properties such as luminescence or high nonlinear optical (NLO) efficiency through the high polarizability of $\pi$-conjugated molecules such as polyene or aromatic compounds (4). These organic phases possess other advantages such as unlimited molecular engineering and often high laser damage thresholds. In addition, large single crystals can be grown in solution close to room temperature as in the case of *N*-4-nitrophenyl-L-prolinol (noted NPP in the following, see Fig. 1), for example (5). Unfortunately, the use of organic crystals for optical applications is generally limited by their insufficient chemical stability, weak thermal stability, and mechanical resistance. An additional drawback is the polar nature of these phases associated with one- or two-dimensional structures. This leads to important problems in crystal growth and processing of optical devices. In order to avoid these basic drawbacks and to take advantages of the optical properties of organic crystals at the nanometer scale, we have recently developed a new strategy based on the nucleation and growth of organic nanocrystals in sol–gel matrices (6–8). We selected sol–gel matrices due to their high stability (chemical, thermal, and mechanical), convenient shaping, and good optical properties (9). Moreover, since 1984 (10), it has been widely shown that the sol–gel method can be used to encapsulate organic molecules in inorganic matrices (bulk or thin films). The flexibility of sol–gel chemistry, involving silicon alkoxides as precursors, and the ability to prepare stable inorganic matrices close to room temperature are compatible with a wide variety of dyes. Until now, molecules were dispersed within or grafted onto sol–gel networks (10–12). In our works, the molecules form aggregates through the confined nucleation of the organic phase in the pores of the gel matrix. This leads to the preparation of a new type of

[1]To whom correspondence should be addressed. Fax: (33) 4 76 88 10 38.



0022-4596/02 $35.00

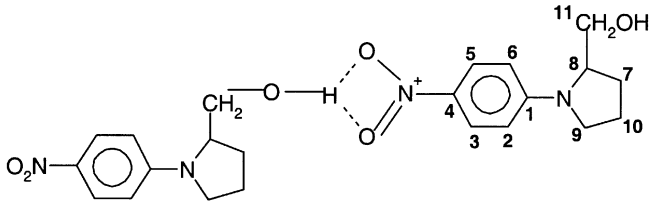


**FIG. 1.** Two *N*-(4-nitrophényl)-(L)-prolinol (NPP) molecules linked by hydrogen bonds in bulk crystal [1] lying between nitro groups and the alcohol functions of NPP chromophores. The numbers are related to the different carbon atoms probed by solid NMR experiments (see Section 4).

hybrid organic–inorganic materials constituted of organic nanocrystals (10–20 nm) dispersed in an amorphous silicate matrix. These nanocomposite compounds not only combine the optical properties of organic phases (NLO, fluorescence, photochromism, etc.) with those of amorphous inorganic materials (high stability, convenient processing, and shaping), but also the advantages of nanocrystals (nanometer-scale effects, photostability). The first advantage of the nanocrystal size is to obtain a nondiffusing sample under a laser beam. Moreover, a confinement of the molecular exchange interaction should lead to an enhancement of optical nonlinearities (13,14). We have recently obtained high third-order NLO efficiency with nanocrystals of stilbene 3 leading to the preparation of potential optical power limiters (15).

We have choosen in this basic study NPP as chromophore because it exhibits, in its bulk crystal form, high quadratic NLO efficiency (16, 17). We have specified the experimental conditions of the nanocrystallization of NPP in sol–gel matrices in order to characterize then the optical properties (luminescence and absorption spectroscopies, NLO efficiency, etc.) of nanocrystals and compare them with those of bulk crystals.

We present in this paper the first results obtained on the preparation of NPP nanocrystals dispersed in bulk xerogels. The crystallinity and thermal stability were characterized by differential scanning calorimetry, and the nanocrystal–matrix interactions were specified through Raman and NMR spectrocopies.

## 2. PREPARATION OF NPP NANOCRYSTALS IN BULK GEL–GLASSES

The preparation of organic nanocrystals in bulk gel–glasses is based on the control of the nucleation and growth kinetics of the dye confined in the pores of dense gels. Our process starts from homogenous solutions containing the dye, the solvent, the silicon alkoxide precursors of the gel, and a small amount of water for the hydrolysis of the alkoxides. Typical polymeric gels were prepared from tetramethoxysilane (TMOS) according to the literature procedure (9). Nevertheless, the resulting silicate network exhibits silanol functions (≡SiOH) which can form hydrogen bonds with the organic molecules and disturb their aggregation (see the following sections). In order to minimize these interactions, methyltrimethoxysilane (MTMOS) was added to the TMOS precursor. That way, gel–glasses of high optical quality were obtained from 0.4TMOS + 0.6MTMOS molar mixtures. The nonbridging methyl functions, arising from MTMOS, cover the gel pores and screen the silanol functions (18, 19). The resulting Van de Waals bonds between the dye and the sol–gel matrix reduce the chromophore–matrix interactions and lead to a significant improvement of the nanocrystallization of the organic phase as illustrated in a previous work (7).

The initial solutions and the NPP powder were placed in airtight silica cells and heated at 80°C in order to rapidly dissolved the dye. The dye concentrations were specified by the molar ratio $d$ = [dye]/[silicon alkoxides]. For TMOS and 0.4TMOS + 0.6MTMOS matrices $d$ was adjusted to $5.8 \times 10^{-2}$ and $6.5 \times 10^{-2}$, respectively. Homogeneous sols were obtained within a few minutes and formed gels after several hours. Gelation occurred in a one-step hydrolysis and condensation process, after 4 h for the TMOS precursor and 2 h for the mixed 0.4TMOS + 0.6MTMOS precursors. These reactions were carried out under acidic conditions (HCl, pH 1.5) with 1 $H_2O$ molecule per alkoxide ($-OCH_3$) function ($h = [H_2O]/[OCH_3] = 1$). Acetonitrile was used to dissolve the dye and to make miscible the water of hydrolysis with the silicon alkoxides. We specified the solvent concentration by the molar ratio $s$ = [solvent]/[alkoxide functions], which was set to 1. The gels were then aged at 80°C for 48 h. This syneresis step made it possible to adjust the gel porosity (centered on 1 nm for these experimental conditions) (20) and to reduce the frequency of crack formation during the drying step (9). Then the nucleation of the organic phase was induced in the pores of the gel which acted as nanometer-scaled reactors of crystal growth in solution. This nucleation in confined solution is only possible at high supersaturations since the mass transport only occurs by diffusion (21, 22). Such high supersaturations were achieved by dropping the temperature from 80 to 25°C. The corresponding relative supersaturation, which depends on the NPP concentration C and its solubility Cs, is given by $\sigma = (C-Cs)/Cs$. For our experimental conditions $\sigma$ was around 1.6. This very high $\sigma$ value, at the initial stage of the process, led to the rapid formation of a high number of NPP nuclei. This burst of nucleation lowered significantly $\sigma$ and thus ended rapidly the nucleation step and limited the subsequent growth stage. Moreover, in these dense gels the growth rate of NPP nuclei was strongly reduced by the slow-diffusion coefficient of molecules, even at high supersaturation. This made it possible to dissociate the nucleation from the particle

growth. Indeed, nucleation occurred in a well-controlled step of short duration during which the growth of the nuclei was negligible. Then, in a second step, the slow growth of nanocrystals occurred during the gel drying without additional nucleation while the dense matrix prevented the NPP nanocrystals from coalescing. Thus, high supersaturation resulted in a fast nucleation well separated from the slow diffusion-controlled particle growth. This process, which is based on La Mer's diagram (23), leads to narrow size distributions of the nanocrystals (10–20 nm), which are characterized by transmission electron microscopy and small angle neutron scattering (20).

In order to obtain monolithic xerogels without cracks, the samples were slowly dried at room temperature for 6 and 4 weeks for TMOS and 0.4TMOS + 0.6MTMOS matrices, respectively. Finally, the samples were annealed at temperatures close to the melting point of the organic phase, around 110°C. Annealings made it possible to improve the crystallinity of the NPP nanocrystals, to remove the remaining solvent, and to stabilize the nanocomposite materials. The resulting monolithic samples exhibit high optical quality as they contain NPP nanocrystals (10–20 nm) and pores (1 nm) too small to scatter the light in the visible region (20). These nanocomposite samples obtained from TMOS and 0.4TMOS + 0.6 MTMOS precursors are labeled as NPP/TMOS and NPP/TMOS + MTMOS, respectively.

## 3. DIFFERENTIAL SCANNING CALORIMETRY

We performed DSC measurements with a Netzsch DSC 404 S equipment. The samples of NPP/TMOS and NPP/TMOS + MTMOS were small pieces (a few cubic millimeters) of xerogels instead of powders. Indeed, the samples were not ground to avoid the amorphization of the organic particles. They were introduced in aluminum caps, and the DSC measurements were carried out with a heating rate of 1 K/min and under an argon flow to avoid the dye oxidation. Figure 2 shows the DSC curve of NPP/TMOS and the NPP/TMOS + MTMOS samples compared to that of NPP powder. The strong endothermic peaks corresponding to the melting of the NPP prove that the aggregates in the amorphous matrices are nanocrystals. Nevertheless, the melting point of these nanocrystals is measured 51°C above that of the pure NPP powder (116°C).

This important thermal stabilization of the nanocrystals in comparison to the pure NPP powder could have two different origins: a chemical modification of the NPP molecules during the nanocrystallization process or an influence of the inorganic matrix. We first considered a modification of the NPP molecules. Indeed, in order to obtain polymeric gels from the alkoxide precursors, the NPP molecules were kept for several days in confined solutions at low pH values (around 1.5) and at temperatures (80°C) close to the NPP melting point. In order to determine whether the nanocrystallization process chemically modifies the organic molecules and to characterize the dye–matrix interactions, we characterized the nanocomposite samples by Raman and NMR spectroscopies.

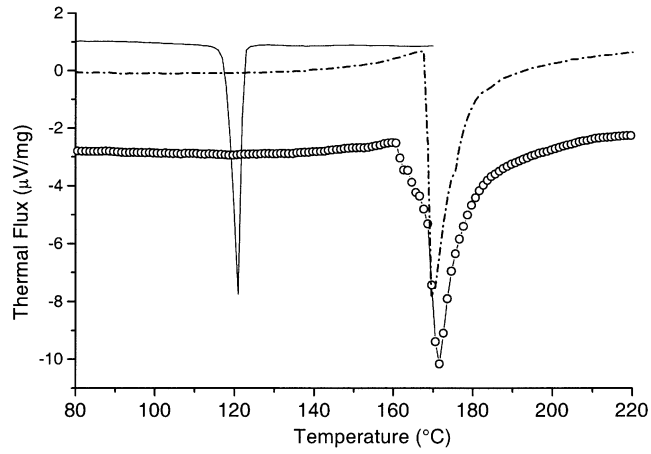


**FIG. 2.** Differential scanning calorimetry curves obtained for the NPP powder and nanocrystals grown in TMOS and in 0.4TMOS + 0.6MTMOS matrices.

## 4. MICRO-RAMAN SPECTROSCOPY

In order to increase the Raman signal of the embedded nanocrystals, we used micro-Raman spectroscopy, which makes it possible to reach high incident intensities by tightly focusing the laser excitation on the sample. Raman measurements were performed on Kaiser Optical Systems HoloProbe (HoloLab Series 5000) instruments. The basic Holoprobe system has been described in detail elsewhere (24). The system incorporates an f/1.8 imaging spectrograph, a thermoelectrically cooled (−40°C) CCD detector (Princeton Instruments), and a high-power laser diode, with an external cavity, which is wavelength-stabilized at 0.785 μm. An Olympus BX60 microscope focuses the laser excitation, collects the backscattered light, and analyzes it with a Raman spectrograph (spectral resolution of 4 $cm^{-1}$). We have taken special care in the choice of the excitation wavelength to reduce, as much as possible, the strong luminescence of NPP molecules, which occurs in the region 0.45–0.7 μm. By selecting $\lambda = 0.785$ μm as excitation wavelength, we were able to avoid the maximum of the luminescence band centered at 0.520 μm and to measure the Raman signal of the organic nanocrystals. Samples of high optical quality were prepared for the different types of sol–gel matrices, with and without NPP nanocrystals, by cutting and polishing plates with parallel faces. Their

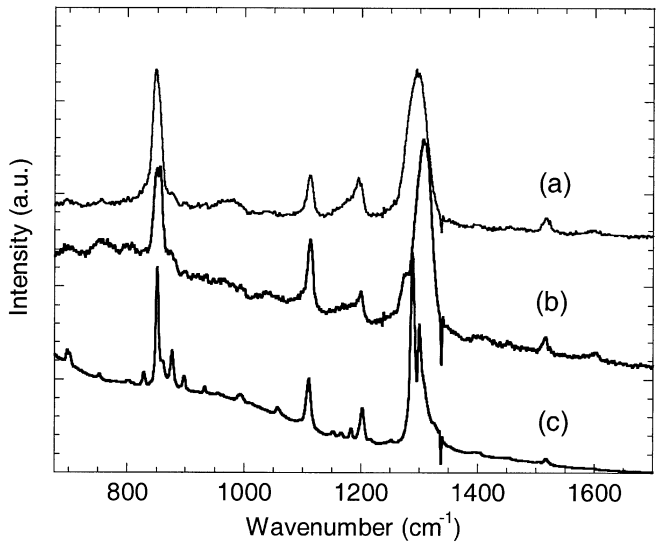


**FIG. 3.** Comparison between the Raman spectrum of NPP powder (c) and those of nanocrytals grown in TMOS (a) and in TMOS + MTMOS xerogels (b).

typical dimensions were $10 \times 5\,mm^2$ and 4 mm thick. Moreover, the Raman spectra of pure NPP powder were measured on a commercial powder (Aldrich, purity grade 99%) with a gain size below 10 μm in diameter.

Figure 3 shows the Raman spectrum of pure NPP powder compared to those of nanocrystals grown in TMOS and TMOS + MTMOS xerogels. The intensity measured for the powder being significantly higher than those measured for nanocrystals due to higher NPP concentration, it has been arbitrarily reduced in this figure for clarity. In addition, an offset was added to the NPP/TMOS and NPP/TMOS + MTMOS spectra to make easier the comparisons. As can be seen in Fig. 3, Raman bands are clearly visible in all cases above the decreasing luminescence of NPP molecules. In the crystallized powder spectrum, the bands are well defined and were identified on the basis of the NPP molecular structure (25), see Table 1. In the two other spectra, corresponding to nanocrystals, the main Raman bands of the NPP molecular are observed (Table 1) but the weakest bands do not appear due to the low signal/noise ratio (low NPP concentrations). Nevertheless, one can see that the same bands appear in the NPP powder spectrum and in the spectra of the organic nanocrystals. These bands are located at almost the same wavenumbers (Table 1), and extra structures are not observed for nanocrystals. This indicates that the same chemical functions and molecular conformations are found in NPP nanocrystals and in the NPP powder. Thus, it seems that NPP molecules are not modified during the nanocrystallization process in TMOS and TMOS + MT MOS sol–gel matrices.

In order to specify the contribution of the sol–gel matrices to the Raman spectra and to characterize the inorganic matrices, Raman spectra of pure xerogels, without NPP nanocrystals, were also measured. They are shown in Fig. 4, where also an offset is added to make easier the comparison between these two spectra. They both exhibit typical bands of silica-based xerogels: the bands at about 460 and 800 $cm^{-1}$ are related to the motion of the oxygen atoms in the Si–O–Si–O network (26, 27) (Table 2). On the other hand, these spectra differ by several aspects related to the precursors used for their elaboration. Indeed, the spectrum of the TMOS xerogel (Fig. 4a) shows a significant band at 975 $cm^{-1}$, which is absent in the TMOS + MTMOS spectrum (Fig. 4b). This structure is

**TABLE 1**
**Raman Bands Observed for the NPP Microcrystalline Powder and for Nanocrystals Grown in TMOS and TMOS + MTMOS Xerogels**

| Band positions ($cm^{-1}$) | | | |
|---|---|---|---|
| Powder | Nanocrystals grown in TMOS | Nanocrystals grown in TMOS + MTMOS | Identification |
| 698 | 696 | 696 | $NO_2$ wag |
| 750 | 754 | 752 | In plane, out of plane *cis* CH wag in prolinol ring |
| 828 | — | — | H wag of *para*-substituted ring |
| 850 | 848 | 852 | $NO_2$ scissors |
| 934 | — | — | Stretch-bisubstituted ring |
| 993 | — | — | *Para*-substituted ring semicircle stretch |
| 1058 | — | — | In plane CH deformation in prolinol ring |
| 1111 | 1112 | 1111 | *Para*-substituted ring semicircle stretch |
| 1151–1165–1181 | Unresolved | Unresolved | In plane CH bend of *para*-substituted ring |
| 1200 | 1200 | 1200 | In phase aryl-$C_2$ stretch mixed with in phase ring contraction |
| 1287 | 1293 | 1305 | C–N stretch in prolinol ring |
| 1300 | Unresolved | Unresolved | O–H bend in prolinol substituant, shoulder: $NO_2$ symmetric stretch |
| 1517 | 1516 | 1513 | $NO_2$ asymetric stretching and semicircle stretch of parasubstituted ring |

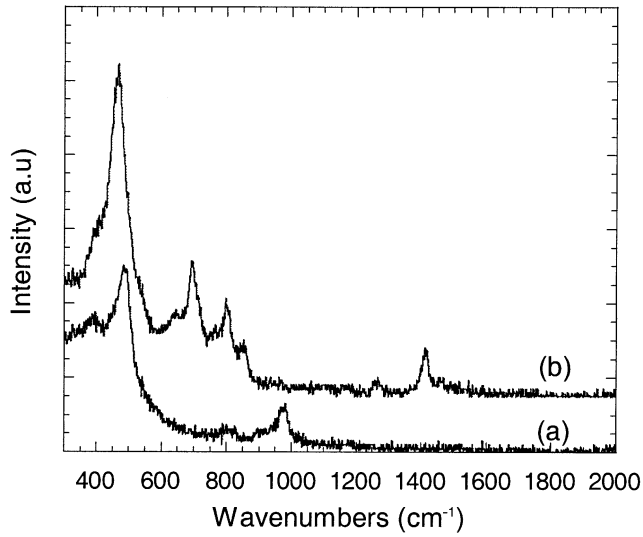


**FIG. 4.** Raman spectra of xerogel matrices without NPP nanocrystals: the TMOS/MTMOS xerogel spectrum (b) is above that of TMOS (a).

assigned to the Si–O stretching of the Si–OH function rather than the stretching of the oxygen atoms in Si–O–Si (commonly found in silica-based sol–gel materials): First, because in the latter case this band would be visible in both spectra and, secondly, because the shoulder usually associated with the Si–O–Si stretching and located at about 1200 $cm^{-1}$ is absent in both spectra. The presence of this structure only in the TMOS xerogel spectrum tends to prove that a significant part of the silanol functions was not condensed during the syneresis of the TMOS gel. On the other hand, the TMOS + MTMOS xerogel spectrum exhibits four additional bands when compared to the TMOS xerogel one. These bands are related to the methyl groups (Table 2), arising from the MTMOS precursor, which are not hydrolyzed during the polymerization of the matrix. Thus, these Raman spectra show an important difference in the structure of the two sol–gel matrices: the xerogels elaborated from TMOS precursors contain a significant amount of silanol functions while those based on TMOS + MTMOS do not show residual silanol functions but methyl groups instead. Indeed, the kinetics of hydrolysis and condensation reactions of the MTMOS precursor, partially substituted with methyl groups, are increased in comparison to the nonsubstituted one (TMOS) (9,18). Thus, similar experimental conditions lead to a more advanced condensation for the TMOS + MT MOS matrix than that for TMOS and then to a much smaller amount of uncondensed silanols. This difference in the amorphous matrix structure can influence the NPP nanocrystals. Indeed, the nonbridging silanol and methyl groups point toward the inside of xerogel pores where they can interact with the organic molecules of the nanocrystals. These interactions will be stronger when silanol functions are involved than when methyl groups cover the pores. Indeed, the silanol functions can make short hydrogen bonds with the organic nanocrystals, through the nitro group of the NPP molecules, for example, while the methyl groups will promote Van der Walls interactions. The resulting stress on the NPP nanocrystals is consistent with the observation of a slight shift toward higher frequencies of several Raman bands of the nanocrystals grown in both matrices when compared to those of the NPP powder (Figs. 3b and 3c, Table 1).

**TABLE 2**
**Raman Bands Observed for the TMOS and TMOS/MTMOS Xerogels without NPP Molecules**

| Band position ($cm^{-1}$) | | |
|---|---|---|
| TMOS | TMOS/MTMOS | Identification |
| 482 | 463 | O rock perpen dicular to the Si–O–Si plane |
| — | 692 | Si–C stretch inSi–$CH_3$ |
| 804 | 800 | O sym. stretch along the bisector of Si–O–Si |
| — | 847 | $CH_3$ rock |
| 975 | — | Si–O stretch in Si–OH |
| — | 1263 | $CH_3$ sym. stretch |
| — | 1414 | $CH_3$ asym. stretch |

Since the thermal stabilization of the NPP nanocrystals (Fig. 2) cannot be explained by a chemical change of the organic molecules, we considered the possible influence of the sol–gel matrices through interactions between the nanocrystals and the silanol or methyl groups covering the inside of the pores. In order to specify such interactions we have undertaken solid state NMR characterizations.

## 5. SOLID STATE $^{29}$SI, $^{1}$H, AND $^{13}$C NMR SPECTROSCOPY

The magic angle spinning (MAS) technique is essential and makes it possible to obtain highly resolved $^{29}$Si NMR spectra for silicates. The simultaneous application of high-power dipolar $^{1}$H decoupling is helpful in removing residual dipolar interaction of $^{29}$Si spins with nearby $^{1}$H nuclei (28). The MAS technique associated with the dipolar decoupling leads to the line-narrowing effect that results in an important improvement of the signal-to-noise ratio of NMR spectra. In addition, the intensities of the $^{29}$Si peaks can be significantly enhanced by using the $^{1}$H–$^{29}$Si cross-polarization technique (CP) when $^{1}$H nuclei exhibit a good polarization transfer to $^{29}$Si. In silicates, the best candidates for CP among the protons are those of Si–OH groups (29–31).

$^{29}$Si NMR spectra were recorded at 59.63 MHz on a MSL 300 spectrometer. Single-pules $^{29}$Si{$^{1}$H} experiments were performed under the following conditions: pulse width 1.4 μs, repetition time 60 s, rotation frequency 4 kHz,

and RF decoupling power of 62.5 kHz. $^{1}H$–$^{29}Si$ CPMAS experiments were performed under the following conditions: pulse width 4.0 μs, contact time 0.1 to 3 ms, repetition time 8 s, rotation frequency 4 kHz, and $^{1}H$ RF field of 62.5 kHz. The samples used were bulk xerogels crushed in pieces of a few cubic micrometer in size which were placed in a 7-mm rotor spinning at the magic angle of 54°44′. Chemical shifts of silicon were referenced to tetramethylsilane (TMS) using Q8M8 (trimethylsilyl ester of cubic octameric silicate) as secondary standard, which appears at −109.7 ppm.

The chemical shifts of the peaks are the most informative parameters in structural studies of silicates by $^{29}Si$ NMR since they reflect very sensitively the structural surroundings of silicon atoms. In this case, the main features, labeled $Q^n$, correspond to the number, $n$, of O–Si atom pairs bonded to the Si probed atom (32, 33). High-field shifts are observed in solid silicates with increasing polymerization of the $Q^n$ species. Table 3 summarizes the five sorts of silicates species that can be found in silica xerogels obtained from TMOS. The $^{29}Si$ MAS spectrum of the NPP/TMOS xerogel (Fig. 5a) associated with the $^{1}H$ decoupling exhibits three peaks: −91.5, −101.2 and −109.5 ppm which are assigned to $Q^2$, $Q^3$, and $Q^4$ species. Their deconvolution leads to 9, 46, and 45% for the $Q^2$, $Q^3$, and $Q^4$ contributions, respectively. CP measurements (Fig. 5b) with contact times from 2 to 0.1 ms confirm the $Q^2$, $Q^3$ and $Q^4$ assignments. When the contact time is lowered, a significant decrease of the $Q^4$ peak is observed because the cross-polarization dynamic is weak due to the distancing of protons from the most condensed silicate species ($Q^4$). On the other hand, $Q^0$ and $Q^1$ peaks, corresponding to species close to the TMOS precursor, are not observed while the $Q^2$ amount is rather weak. This indicates a high advancement of the hydrolysis and condensation reactions even if residual silanols functions remain in the xerogels ($Q^2$, $Q^3$ species). These Si–OH groups can establish hydrogen bonds with the NPP molecules, particularly through their nitro functions (Fig. 1).

Figure 6 shows CP spectra of the NPP/TMOS + MTMOS xerogel involving the $^{1}H$ decoupling with contact times of 3 and 1 ms. These spectra exhibit like the previous ones highly condensed species, $Q^3$ (–100.64 ppm) and $Q^4$ (–109.43 ppm) arising from the TMOS alkoxide. In this case, the peak corresponding to the $Q^2$ species, around –91

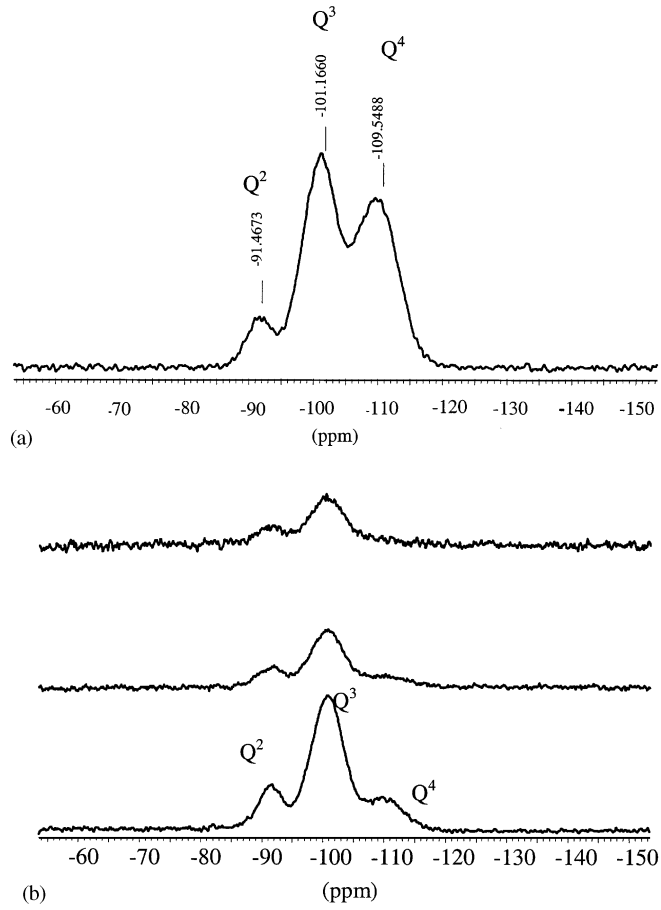


**FIG. 5.** (a) The $^{29}Si$ MAS technique associated with the $^{1}H$ decoupling applied to the NPP/TMOS xerogels. (b) The $^{29}Si$ MAS technique associated with the $^{1}H$ decoupling applied to the NPP/TMOS xerogels with different contact times ($t_c$ = 0.1 ms at the top, $t_c$ = 0.5 ms in the middle, and $t_c$ = 2 ms at the bottom).

**TABLE 3**
**Chemical Shift of Different Chemical Species Observed in $^{29}Si$ NMR**

| Species | Chemical shift (ppm) |
|---|---|
| $Q^0$: $Si(OCH_3)_x\ (OH)_{4-x}$, $0 \le x \le 4$ | −79–73 |
| $Q^1$: $Si(OSi)(OCH_3)_y(OH)_{3-y}$, $0 \le y \le 3$ | −86–82 |
| $Q^2$: $Si(OSi)_2\ (OCH_3)_z\ (OH)_{2-z}$, $0 \le z \le 2$ | −91–95 |
| $Q^4$: $Si(OSi)_3\ (OCH_3)_t\ (OH)_{1-t}$, $0 \le t \le 1$ | −99–103 |
| $Q^4$: $Si(OSi)_4$ | −110 |

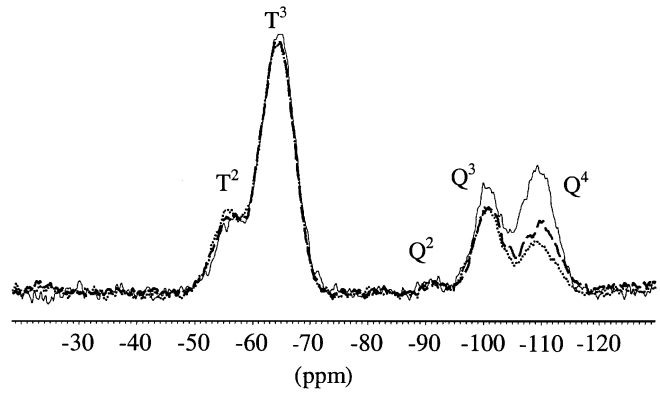


**FIG. 6.** The $^{29}Si$ CP/MAS technique associated with the $^{1}H$ decoupling applied to the NPP/TMOS + MTMOS xerogel with a contact tome of 3 ms (dotted line) and 1 ms (solid line).

ppm, is very small. On the other hand, the MTMOS precursor gives two other contributions $T^2$ (–55.96 ppm) and $T^3$ (–64.41 ppm), corresponding to the chemical species $CH_3Si(OSi)_2(OH)$ and $CH_3Si(OSi)_3$, respectively. Spectra deconvolution gives $11.4\%(T^2)+48.6\%(T^3)=60\%$ and $23.6\%\ (Q^4)+16.4\%\ (Q^3)=40\%$, corresponding to MTMOS and TMOS amounts. In the NPP/TMOS + MT MOS sample, the $Q^4/Q^3$ ratio (1.44) corresponding to condensed species is higher than that observed for NPP/ TMOS (0.99). These measurements show a higher cross-linking of the Si–O–Si polymerization in NPP/ TMOS + MTMOS than in NPP/TMOS. Indeed, the methyl group, through the inductive electrodonnor effect, enhances hydrolysis and condensation reactions (9). Thus, $^{29}$Si NMR measurements show clearly that the Si–OH amount is lower in NPP/TMOS + MTMOS than in NPP/ TMOS samples. This result is in agreement with Raman spectroscopy and with a decrease of the dye–matrix interactions when MTMOS is added. Then, in order to identify these interactions between NPP molecules and the matrix, we performed $^1$H and $^{13}$C NMR measurements.

$^1$H and $^{13}$C NMR spectra were recorded on a MSL 300 spectrometer at 300.13 and 75.43 MHz, respectively. Single-pulse $^1$H experiments were carried out with a $\pi/2$ pulse width of 4 μs and recycle delays of 8 s. For $^1$H/$^{13}$C cross-polarization experiments the initial $^1$H $\pi/2$ pulse width was 4 μs with Hartmann–Hahn matching periods of 1 ms and recycle delays of 5 s. The samples were spinned at 4 kHz at the magic angle.

Figure 7 shows the $^1$H MAS spectra of NPP/TMOS and NPP/TMOS + MTMOS xerogels. These spectra are mainly constituted by a main peak at 4.5 ppm, corresponding to the OH group of the NPP prolinol function and a smaller one at 7.2 ppm (shoulder of the previous peak) arising form aromatic protons. The peak at 0.2 ppm corresponds to the methyl groups of the MTMOS precursor. The other structures, corresponding to rotation bands, are more numerous for the NPP/TMOS + MTMOS sample. These rotation bands are assigned to NPP molecules located at he surface of nanocrystals and are thus directly related to their rigidity. Indeed, when the MTMOS precursor is involved in the inorganic matrix, the Si–OH groups are less numerous and screened by the methyl ones. This decreases the number of hydrogen bonds between nanocrystals and the host matrix and thus reduces the rigidity of the NPP molecules at the surface of the nanocrystals. Moreover, the full-width at half-maximum (FWHM) of the peaks are higher for NPP/TMOS (900 Hz) than for NPP/ TMOS + MTMOS (450 Hz). The broadening of these peaks for NPP/TMOS is certainly related to several conformations of NPP molecules existing in the crystal structure, at the particle surface, and also through the weak amount of dispersed molecule in the sol–gel matrix. This later amount of not aggregated NPP Molecules, higher in NPP/TMOS than in NPP/TMOS + MTMOS, corresponds to a higher FWHM of the peaks.

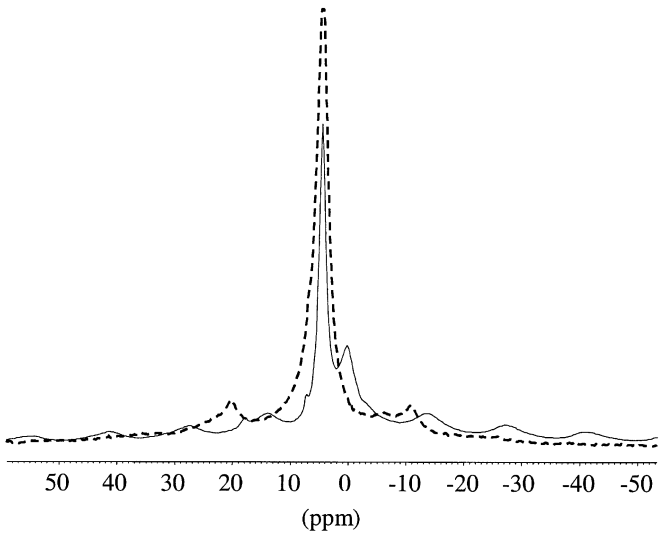


**FIG. 7.** $^1$H MAS spectra for NPP/MOS (dashed line) and NPP/ TMOS + MTMOS (solid line) xerogels.

$^{13}$C cross-polarization NMR spectra of NPP/TMOS (Fig. 8a) and NPP/TMOS + MTMOS (Fig. 8b) are compared to that of the NPP microcrystalline powder. All the different $^{13}$C nuclei of NPP (labeled in Fig. 1) are found both in the NPP power and in the nanocomposite samples (Fig. 8 and Table 4). As for proton spectra, we observe a significant broadening of the peaks due to several conformations of NPP molecules (Figs. 8a and 8b). In order to characterize the carbon mobility, particularly that of the C(4) and C(11) atoms (Fig. 1), and to dissociate the NPP intermolecular interactions from the dye–matrix ones, we performed dipolar dephasing experiments. This experiment consists of a normal cross-polarization period followed by the insertion of a short delay (50 μs) in which both $^{13}$C and $^1$H RF fields are turned off before the $^1$H field is turned back on and the data acquisition begins. During the delay period, the $^{13}$C spins precess in their local proton dipolar fields. For carbons subject to strong C–H dipolar coupling, the signal quickly decays. The resulting spectrum therefore consists mainly of signals arising form nonprotoned carbons or molecules in a liquid-like, noncrystalline component (involved in a high molecular dynamic). Figures 9a and 9b show the $^{13}$C CP and dipolar dephasing measurements for NPP/TMOS and NPP/TMOS + MTMOS, respectively. In both samples, the peaks of C(3), C(5), C(2), and C(6) nuclei (aromatic ring, Fig. 1) and those of C(8), C(11), C(10), and C(7) completely disappear in the dipolar dephasing spectra due to the molecular rigidity. Moreover, the disappearance of the C(11) peak in both nanocomposite samples is the result of intermolecular interactions between alcohol and nitro groups in NPP

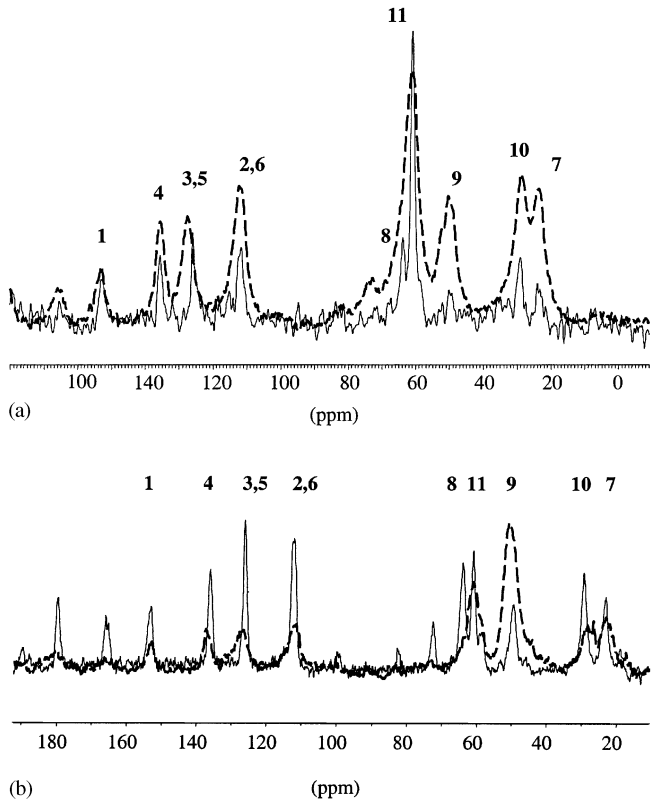


**FIG. 8.** (a) $^{13}C$ CP/MAS + $^{1}H$ decoupling spectra of NPP/TMOS xerogel (dashed line) compared to NPP microscrytalline powder spectrum (solid line). The numbers correspond to the NPP carbon atoms shown in Fig. 1. (b) $^{13}C$ CP/MAS + $^{1}H$ decoupling spectra of NPP/TMOS + MT MOS xerogel (dashed line) compared to NPP microscrytalline powder spectrum (fine line). The numbers in the figure correspond to carbon atoms presented in Fig. 1 of the NPP molecule.

nanocrystals as previously observed in the bulk crystal structure of NPP (34). This confirms that the great majority of NPP molecules in these nanocomposite materials are aggregated in nanocrystals. On the other hand, the main differences observed in Fig. 9 between the two samples are focused on the C(4) and C(1) peaks, which are more reduced in the TMOS matrix than in the TMOS + MT-MOS one when the dipolar dephasing is applied. This means that the C(4) and C(1) atoms are involved in a lower molecular dynamic in NPP/TMOS than in NPP/TMOS + MTMOS due to higher nanocrystal–matrix interactions. These interactions are hydrogen bonds between the NPP molecules at the nanocrystal surface and the silanols of the TMOS matrix. On the other hand, the peak centered at 50 ppm corresponds both to the C(9) of NPP and to the carbon of methanol. Indeed, methanol is produced by the hydrolysis and condensation reactions of TMOS and MTMOS. When MTMOS is involved, the condensation of the silicate network is enhanced, leading to the encapsulation of methanol molecules in the interconnected network. For this reason, the peak at 50 ppm does not disappear in the dipolar dephasing spectrum of NPP/TMOS + MTMOS (Fig. 9b).

**TABLE 4**
**Chemical Shift of Different Chemical Functions Observed by $^{13}C$ NMR in NPP Organic Dye**

| Carbon atom numbered in Fig. 1 | Chemical shift (ppm) |
|---|---|
| C(1) | 152.9067 |
| C(4) | 135.9528 |
| C(3), C(5) | 126.0259 |
| C(2), C(6) | 111.8605 |
| C(8) | 63.8432 |
| C(11) | 60.8317 |
| C(9) | 49.2874 |
| C(10) | 29.2105 |
| C(7) | 22.9643 |

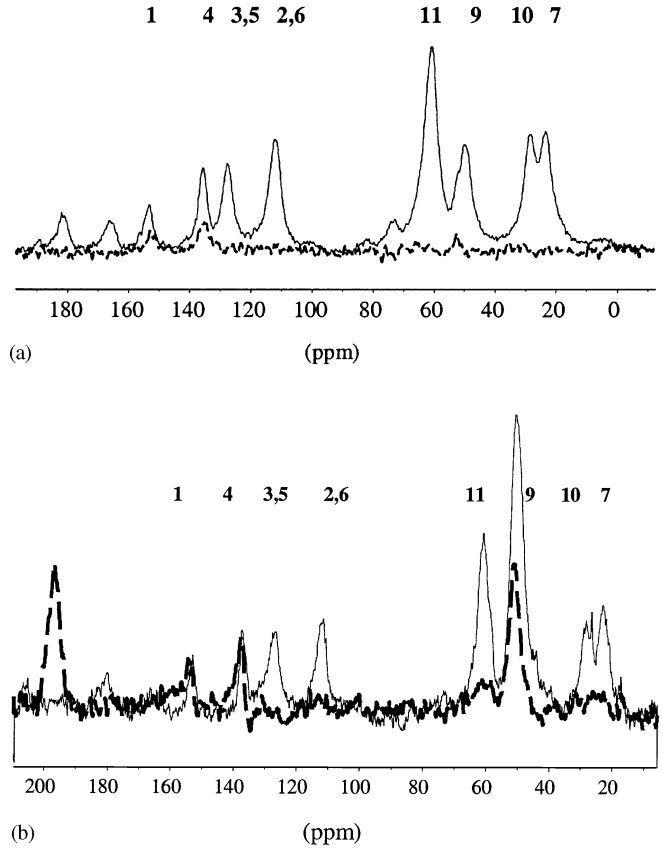


**FIG. 9.** (a) The $^{13}C$ CP/MAS experiment (fine line) and the dipolar dephasing spectrum (dashed line) of the NPP/TMOS xerogel. The numbers in the figure correspond to carbon atoms presented in Fig. 1 of the NPP molecule. (b) The $^{13}C$ CP/MAS spectrum (fine line) compared to the dipolar dephasing spectrum (dashed line) of the NPP/TMOS + MT MOS xerogel. The numbers in figure correspond to carbon atoms presented in Fig. 1 of the NPP molecule.

## 6. CONCLUSION

In this study we have prepared NPP nanocrystals grown in sol–gel matrices through the control of nucleation and growth kinetics. The melting point of these nanocrystals (10–20 nm) is 51°C above that of NPP powder. Micro-Raman and solid state NMR spectroscopies allowed us to demonstrate that NPP molecules are not chemically modified by our nanocrystallization process. In addition, these coupled characterizations specified also the interactions existing between the NPP noncrystals and the xerogel. Thus, the important thermal stabilization observed by DSC for nanocrystals in comparison to pure NPP powder is due to hydrogen bonds between the nitro groups of NPP molecules located at the particle surface and the uncondensed silanol functions of the silicate network. Similar behaviors have been observed for nanocrystals of other organic molecules containing nitro groups (35). Moreover, the melting peak of the NPP/TMOS xerogel is larger ($\Delta T = 25°C$) than that of NPP/TMOS + MTMOS ($\Delta T = 22°C$, Fig. 2). This is due to a lower crystallinity of NPP nanocyrstals in the case of the TMOS matrix due to a higher number of dye–matrix hydrogen bonds through silanols, which are not partially screened by nonbridging methyl groups as in the 0.4TMOS + 0.6MTMOS xerogel. This high number of hydrogen bonds between NPP molecules and the silicate network can disturb the dye aggregation as previously evidenced (7). Nevertheless in this study, even for the NPP/TMOS sample, the well-defined melting peaks (Fig. 2) demonstrate the good crystallinity of NPP aggregates in the sol–gel matrix. This result is in good agreement with $^{13}C$ NMR measurements which show that intermolecular interactions in NPP nanocrystals are very similar to those of bulk crystal and that the great majority of NPP molecules are aggregated in nanocrystals in these hybrid nanocomposite materials.

Luminescence and absorption spectroscopies of nanocrystals are now in progress. The first quadratic nonlinear optical characterizations show that these first samples, constituted of randomly oriented nanocrystals in amorphous matrices, exhibit second harmonic generation (SHG) effects. This SHG is associated with self-oriented domains of nanocrystals due to dipole–dipole interactions (36). In order to increase the quadratic nonlinear optical properties we are now undertaking the control of the nanocrystal orientation. We have obtained promising results by applying high magnetic (16 T) during the nanocrystallization process. In this case we obtain an oriented growth through the diamagnetic susceptibility of the organic molecules (36). Other works involving thermal treatments in order to melt and then solidify NPP nanocrystals under an electric field are in progress.

## ACKNOWLEDGMENT

The authors thank the Common Center of Optical Microspectrometry of Lyon for the Raman experimental setup.

## REFERENCES

1. R. Reisfeld, "Structure and Bonding," Vol. 85, pp. 99–145. Springer-Verlag, Berlin, 1996.
2. H. S. Nalva, H. Kasai, S. Okada, H. Oikawa, H. Matsuda, A. Kakuta, A. Mukoh, and H. Nakanishi, *Adv. Mater.* **5,** 758–760 (1993).
3. I. A. Akimov, I. Denisyuk, and A. M. Meshkov, *J. Opt. Spectrosc.* **77,** 858–863 (1994).
4. "Nonlinear Optical Properties of Organic Molecules and Crystal," D. S. Chemla and J. Zyss (Eds.), Vols. 1 and 2, Academic Press, Orlando, FL, 1987.
5. B. Y. Shekkunov, E. A. Shepherd, J. N. Sherwood, and G. S. Simpson, *J. Phys. Chem.* **99,** 7130–7136.
6. A. Ibanez, S. Maximov, A. Guiu, C. Chaillout, and P. L. Baldeck, *Adv. Mater.* **10,** 1540–1543 (1998).
7. N. Sanz, A. C. Gaillot, P. L. Baldeck, and A. Ibanez, *J. Mater. Chem.* **10,** 2723–2726 (2000).
8. N. Sanz, P. L. Baldeck, and A. Ibanez, Synth. Met. **115,** 229–234 (2000).
9. C. J. Brinker and G. W. Scherer, "Sol-Gel Science, The Physics and Chemistry of Sol-Gel Processing." Academic Press New York, 1990.
10. D. Avnir, D. Levy, and R. Reisfeld, *J. Phys. Chem.* **88,** 5957–5962 (1984).
11. C. Sanchez and F. Ribot, *New J. Chem.* **18,** 1007–1047 (1994).
12. D. Avnir, V. R. Kaufman, and R. Reisfeld, *J. Non-Cryst. Solids* **74,** 395–406 (1985).
13. F. S. Spano and S. Mukamel, *Phys. Rev. A* **40,** 5783 (1989).
14. H. Ishihara, K. Cho, *Phys. Rev. B* **42,** 1724 (1990).
15. N. Sanz, A. Ibanez, Y. Morel, and P. L. Baldeck, *Appl. Phys. Lett.* **78,** 2569–2571 (2001).
16. J. Zyss, J. F. Nicoud, and M. Coquillay, *J. Chem. Phys.* **81,** 4160–4167 (1984).
17. M. Barzoukas, D. Josse, P. Fremaux, J. Zyss, J. F. Nicoud, and J. O. Morley, *J. Opt. Soc. Am. B* **4,** 977–986 (1987).
18. H. Schmidt, H. Scholze, and A. Kaiser, *J. Non-Cryst. Solids* **64,** 1–11 (1984).
19. H. Scholze, *J. Non-Cryst. Solids*, **73,** 669–680 (1985).
20. N. Sanz, D. Djurado, P. Terech, and A. Ibanez, to be published.
21. F. Lefaucheux and M.C. Robert, *in* "Handbook or Crystal Growth" (D. T. J. Hurle, Ed.), Vol. 2-b, pp. 1271–1303. North-Holland, Amsterdam, 1994.
22. M. Bienfait and R. Kern, *Bull. Soc. Franç. Minér. Crist.* **87,** 604–613 (1964).
23. V. K. La Mer, *J. Am. Chem. Soc.* **72,** 4847–4854 (1950).
24. N. Everall, K. Davis, H. Owen, M. J. Pelletier, and J. Slater, *Appl. Spectrosc.* **50,** 388–393 (1996).
25. D. Lin-Vien, N. B. Colthup, W. G. Fateley, and J. G. Grasselli, "The Handbook of Infrared and Raman Characteristic Frequencies of organic Molecules." Academic Press, London, 1991.
26. F. L. Galeener, *Phys. Rev. B* **19,** 4292–4297 (1979).
27. R. M. Almeida and C. G. Pantano, *J. Appl. Phys.* **68,** 4225–4232 (1990).
28. C. A. Fyfe, "Solid state NMR for chemist." CFC Press, Boca Raton, FL, 1983.
29. G. Engelhardt and D. Michel, "High-Resolution Solid State NMR of Silicates and Zeolithes." John Wiley and Sons, London, 1987.

30. J. F. Stebbins, P. F. McMillan, and D. B. Dingwell, "Structure, Dynamics and Properties of Silicate Melts." Mineralogical Society of America, 1995.
31. L. W. Kelts, N. J. Effinger, and S. M. Melpolder, *J. Non-Cryst. Solid.* **83,** 353–374 (1986).
32. C. A. Balfe and S. L. Martinez *in* "Better Ceramics through Chemistry II" (C. J. Brinker, D. E. Clark, D. R. Ulrich, Eds.), Vol. 73, pp. 27–36, MRS Symposia Proceedings, Pennsylvania, 1986.
33. D. H. Doughty, R. A. Assink, and B. D. Kay, "Silicon-Based Polymer Science: A Comprehensive Resource" (J. M. Zeigler and F. W. Gordon Fearon, Eds.), Vol. 224, 1990.
34. W. Buguo, Z. Weizhuo, Y. Cheng, S. Erwei, and Y. Zhiwen, *J. Cryst. Growth* **160,** 375–381 (1996).
35. N. Sanz, A. Boudet, and A. Ibanez, *J. Nanoparticle Res.*, in press.
36. N. Sanz, I. Wang, J. Zaccaro, E. Beaugnon, P. L. Baldeck, and A. Ibanez, *J. Adv. Funct. Mater.*, submitted.